

JGR Space Physics

RESEARCH ARTICLE

10.1029/2019JA026477

Special Section:

Particle Dynamics in the Earth's Radiation Belts

Key Points:

- Solar wind pressure fluctuations were directly transferred to the magnetosphere and then propagated throughout the magnetosphere
- Global pressure perturbations provided temperature anisotropies that drove EMIC waves throughout the magnetosphere
- Electron precipitation was recorded by the BARREL balloons, although it did not have the same widespread signatures as the wave signatures

Correspondence to:

M. R. Lessard,
marc.lessard@unh.edu

Citation:

Lessard, M. R., Paulson, K., Spence, H. E., Weaver, C., Engebretson, M. J., Millan, R., et al. (2019). Generation of EMIC waves and effects on particle precipitation during a solar wind pressure intensification with $B_z > 0$. *Journal of Geophysical Research: Space Physics*, 124, 4492–4508. <https://doi.org/10.1029/2019JA026477>

Received 8 JAN 2019

Accepted 21 MAY 2019

Accepted article online 29 MAY 2019

Published online 29 JUN 2019

Generation of EMIC Waves and Effects on Particle Precipitation During a Solar Wind Pressure Intensification With $B_z > 0$

Marc R. Lessard¹, Kristoff Paulson¹, Harlan E. Spence¹, Carol Weaver¹, Mark J. Engebretson², Robyn Millan³, Leslie Woodger³, Alexa Halford⁴, Richard Horne⁵, Craig J. Rodger⁶, and Aaron Hendry^{6,7}

¹Space Science Center, University of New Hampshire, Durham, NH, USA, ²Department of Physics, Augsburg University, Minneapolis, MN, USA, ³Department of Physics and Astronomy, Dartmouth College, Hanover, NH, USA, ⁴The Aerospace Corporation, Chantilly, VA, USA, ⁵British Antarctic Survey, Cambridge, UK, ⁶Department of Physics, University of Otago, Dunedin, New Zealand, ⁷Now at Institute of Atmospheric Physics, Czech Academy of Sciences, Prague, Czech Republic

Abstract During geomagnetic storms, some fraction of the solar wind energy is coupled via reconnection at the dayside magnetopause, a process that requires a southward interplanetary magnetic field B_z . Through a complex sequence of events, some of this energy ultimately drives the generation of electromagnetic ion cyclotron (EMIC) waves, which can then scatter energetic electrons and ions from the radiation belts. In the event described in this paper, the interplanetary magnetic field remained northward throughout the event, a condition unfavorable for solar wind energy coupling through low-latitude reconnection. While this resulted in SYM/H remaining positive throughout the event (so this may not be considered a storm, in spite of the very high solar wind densities), pressure fluctuations were directly transferred into and then propagated throughout the magnetosphere, generating EMIC waves on global scales. The generation mechanism presumably involved the development of temperature anisotropies via perpendicular pressure perturbations, as evidenced by strong correlations between the pressure variations and the intensifications of the waves globally. Electron precipitation was recorded by the Balloon Array for RBSP Relativistic Electron Losses balloons, although it did not have the same widespread signatures as the waves and, in fact, appears to have been quite patchy in character. Observations from Van Allen Probe A satellite (at postmidnight local time) showed clear butterfly distributions, and it may be possible that the EMIC waves contributed to the development of these distribution functions. Ion precipitation was also recorded by the Polar-orbiting Operational Environmental Satellite satellites, though tended to be confined to the dawn-dusk meridians.

1. Introduction

Electromagnetic ion cyclotron (EMIC) waves are generated near the geomagnetic equator by anisotropic ($T_{\perp} > T_{\parallel}$) energetic (~ 10 – 100 keV) proton distributions (Cornwall et al., 1970; Horne & Thorne, 1993; Kozyra et al., 1984; Remya et al., 2018). The waves have frequencies that depend on the background ion populations, including effects from heavy ions, thus leading to a solar cycle dependence of wave frequencies (Lessard et al., 2015), following variations in heavy ion densities that follow this trend.

The overlap between hot protons in the ring current and cooler plasmaspheric populations can lower the threshold of generating EMIC waves. While it has been shown in some studies that this is a region where EMIC waves can occur (e.g., see Summers et al., 1998), it is not a preferred location (Allen et al., 2015; Fraser & Nguyen, 2001; Halford et al., 2015; Tetrack et al., 2017), and, in fact, observational studies using satellites and ground instruments have shown that EMIC waves occur at all local times (Anderson et al., 1992; Kuwashima et al., 1981; Usanova et al., 2012).

In addition, EMIC waves can be generated throughout the magnetosphere by velocity fluctuations in solar wind that drive the requisite temperature anisotropies via pressure modulations (Anderson & Hamilton, 1993; Arnoldy et al., 2005; Usanova et al., 2010). Saikin et al. (2015) explored this connection statistically, using data from the Van Allen Probes spanning a 22-month period. EMIC waves that occurred during

this time interval were correlated with storm phases and, separately, with solar wind pressure. Separating EMIC occurrences below and above 3 nPa, they show that the highest occurrence rates (greater than ~35%) occur at prenoon for solar wind pressures below 3 nPa. During times with higher pressures, although the highest rates (near 50%) are concentrated at postnoon, EMIC occurrences are widespread throughout the magnetosphere. Tetrick et al. (2017) found a similar dependence in several local time sectors.

In a detailed study of pressure-driven waves, Engebretson et al. (2015) describe an event that extended over 8 hr in UT and over 12 hr in local time, driven by a 4-hr rise and subsequent sharp increases in solar wind pressure, observed outside the plasmopause from late morning through local noon. Linearly polarized hydrogen-band waves associated with this event were observed with magnitudes up to 25 nT p-p.

Cho et al. (2017) present observations of EMIC waves during two separate pressure enhancements. In the first event, where the pressure reached ~10 nPa, EMIC waves were observed by various spacecraft nearly simultaneously from ~5 to 8 MLT, though no waves were observed by GOES 13 at prenoon (no spacecraft were positioned between noon, dusk, and midnight to ~5 MLT). On the other hand, EMIC waves during the second event were observed postnoon to postmidnight in response to a solar wind pressure that reached 20 nPa.

Dayside pressure-driven EMIC waves were also reported by Engebretson et al. (2018), which were observed by the Magnetosphere Multiscale spacecraft, Van Allen Probe A, and GOES 13 and four ground stations, all concentrated near noon. The solar wind initially provided a modest interplanetary shock, but that was followed by a continued increase in solar wind dynamic pressure that gradually reached and exceeded 10 nPa.

These studies (as well as the event described in this paper) suggest that pressure-driven EMIC waves can occur throughout the magnetosphere, in locations that may differ from occurrence distributions shown in various statistical studies (e.g., described above). Given that radiation belt activity is highly correlated with magnetic storms, high-speed streams, solar wind pressure pulses, and so forth, the implication is that EMIC waves that occur during active times may play a more significant role in radiation belt dynamics than those that fit quiet time occurrence distributions.

The specific role that EMIC waves play in radiation belt dynamics is not clear. EMIC waves are able to pitch-angle scatter protons from the ring current into the loss cone, which can be seen as direct precipitation or as detached proton auroral arcs, either on the ground or by satellites (Cornwall et al., 1971; Jordanova et al., 2007; Sakaguchi et al., 2012; Spasojevic & Fuselier, 2009; Yahnin et al., 2009; Yuan et al., 2010, 2018). There is also expected to be a correspondence between EMIC waves and relativistic electron precipitation (Meredith et al., 2003; Summers & Thorne, 2003), which could lead to large-scale dropouts of radiation belt electrons during the main phase of geomagnetic storms. However, not all electron dropouts can be explained by EMIC waves (Morley et al., 2010), although there are a few experimental observations of EMIC-driven relativistic electron precipitation (e.g., Blum et al. 2015; Hendry et al., 2016, 2017; Miyoshi et al. 2008; Rodger et al., 2008, 2015; Usanova et al. 2014). Compression-driven EMIC waves and their effect on radiation belt electrons, in particular, have been studied from both observations and simulations (McCollough et al., 2009, 2012; Usanova et al., 2008, 2010; Wang et al., 2014).

In the event described in this paper, EMIC wave generation occurred simultaneously throughout nearly all local times, though most predominantly in the dusk and midnight regions. Energetic particle precipitation was also observed on global scales.

2. Observations on 17 January 2013

Geomagnetic storms result from the interaction of the solar wind with Earth's magnetosphere, often with the result that energized particles injected into the inner magnetosphere from the magnetotail enhance currents and also the conditions leading to the growth of EMIC waves.

Satellite measurements have shown that the majority of EMIC waves seen during storms occur during the main phase (Halford et al., 2010) when particle dynamics are at a peak but the majority of waves observed on the ground during storms occur in the late recovery phase (Engebretson et al., 2008). The disconnect between satellite and ground measurements is likely due to waves being unable to propagate through the ionosphere during disturbed conditions (Bräysy et al., 1998). Using Van Allen Probe data, Wang et al. (2016) showed

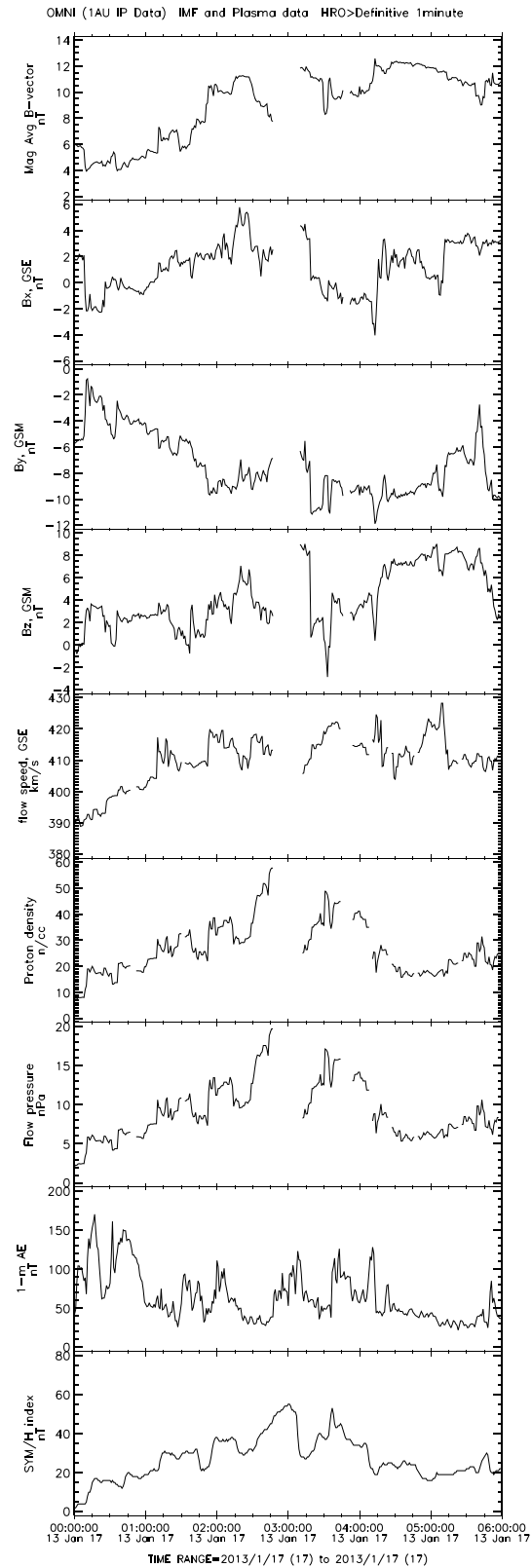


Figure 1. OMNI data showing solar wind parameters associated with this event. The top four panels show total magnetic field strength, followed by B_x , B_y , and B_z . The next three panels show solar wind speed, density, and flow pressure. The bottom two panels show the AE and SYM/H indices.

that during storm main phases, EMIC waves occur primarily in the dusk sector, with peak occurrence rates can approach 30%, while EMIC waves in the recovery phase are distributed more uniformly, with peak occurrence rates near 20% in the dawn to noon sector.

In general, geomagnetic storms are identified by negative excursions in the global D_{st} or SYM/H indices, either of which indicates an intensification of the ring current, which would be driven by coupling of the enhanced solar wind at the dayside subsolar magnetopause. This coupling requires that the solar wind magnetic field includes a negative B_z component to enable the reconnection. On the other hand, when B_z is positive, no notable reconnection takes place, although solar wind pressure perturbations are transferred to the magnetosphere. In typical magnetic storms, the polarity of B_z often changes during the event, resulting in a toggling between the two processes, and so the meaning of “storm” most often includes interpretation of the integrated effects of the toggling.

In the event described in this paper, the solar wind density was very high (up to 58 particles per cubic centimeter), but B_z remained positive throughout the event. With B_z remaining positive, reconnection did not take place at the subsolar point, and the ring current appears to not have been intensified. That is, SYM/H did not undergo a negative excursion in spite of the fact that the solar wind density was so high. In a strict sense, this can be taken to mean that the event is not classified as a magnetic storm, though pressure perturbations certainly were transferred to the magnetosphere.

Such pressure perturbations have been correlated with D_{st} previously (see Francia et al., 1999, and references therein) and are thought to correspond to increases in the Chapman-Ferraro currents at the magnetopause. In fact, Burton et al. (1975) had previously noted the importance of these currents on the D_{st} index and developed an empirical model for predicting D_{st} that included the speed and density of the solar wind, as well as B_z .

The event described here confirms and extends the results from an earlier paper by Engebretson et al. (2015), who also focused on EMIC wave generation that was initiated by pressure perturbations, as opposed to the often-cited overlap between plasmasphere and ring current populations.

On 17 January 2013, a high-density solar wind impacted the magnetosphere. Figure 1 shows the solar wind conditions from 00:00 to 06:00 UT 17 January 2013 from the OMNIWeb database. Data from both the ACE and Wind satellites were used to calculate the OMNI values, except for a brief data dropout around 0300 UT. The top four panels show the magnetic field magnitude and components. Note that B_z is positive for the entire interval, except for a brief and minor negative excursion near 03:30 UT. The fourth panel shows the solar wind speed with values near 410 km/s, which is a typical speed.

The density (fifth panel) and flow pressure (sixth panel), however, show a marked increase starting at 00:00 UT and then reach a maximum of 58 particles per cubic centimeter and 20 nPa, respectively, just as the data become unavailable at 02:47 UT. The AE index (eighth panel) shows low values throughout the interval, implying the presence of ongoing substorms, which is surprising and not expected, given the lack of negative B_z that would support the nightside reconnection generally thought to be required for substorm development.

SYM/H (bottom panel) reaches a maximum value of 55 nT at 0301 UT. Of particular importance is the fact that SYM/H tracks the flow pressure very closely, in an apparently linear fashion (i.e., they are clearly correlated). This is, perhaps, indicative of the fact that energy was not transferred to the ring current via reconnection at the magnetopause, but rather through the sort of direct driving by the solar wind quantified by Kepko and Spence (2003) and Viall et al. (2009). The positive perturbation in SYM/H, in this case, is not related to changes in the ring current, primarily, but to intensified magnetopause currents (Burton et al., 1975)

2.1. EMIC Waves Observed on the Ground

Unlike typical occurrence distributions described in section 1, ground-based observations of EMIC waves during this event were concentrated in the dusk and midnight regions and were excited globally and simultaneously, producing similar spectral signatures at virtually all ground stations. Figure 2 shows the locations of the ground stations and satellites where EMIC waves were observed. Note that the gap between Magadan (eastern Siberia) and Sodankylä (Finland) reflects in large part the lack of search coil coverage over much of Siberia at the time of this event.

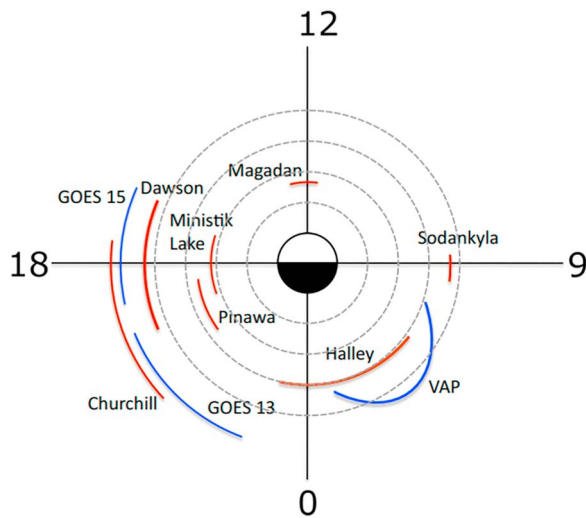


Figure 2. This figure provides the approximate locations of ground-based (red) and space-based (blue) platforms where electromagnetic ion cyclotron waves were observed. The sketch shows coordinates in L and MLT, although signatures at the ground observations are modified by ionospheric ducting. The ducting means that signals will reach the ground stations almost regardless of the latitude at which they were injected into the ionosphere. Thus, assigning an L shell to the stations maybe not be realistic.

Figure 3 shows dynamic spectra of magnetic fluctuations from various stations around the world. The top panel shows data from Halley Station in Antarctica. Other panels show data from Finland, Russia, and Canada, with the order of the plots progressive from east to west in terms of MLT.

An important aspect of the interpretation of ground observations of these waves is that the signals are ducted in the ionosphere. Greifinger (1972; see also Fraser, 1975, and Kim et al., 2011) show that waves at these frequencies can enter the ionosphere and couple energy to compressional waves that are then ducted horizontally in a region centered around the Alfvén speed minimum (i.e., an electron density maximum near ~ 400 km). This results in wave events being observed over a large latitudinal extent (local time spread is also possible but latitudinal spread is more efficient) which, unfortunately, also means that determination of the L shell of the wave injection into the ionosphere is not possible from these data alone.

Panels 4 to 7 show EMIC waves observed on the ground at Canadian Array for Realtime Investigations of Magnetic Activity sites extending from Dawson City, Yukon (magnetic midnight at 10.4 UT) to Fort Churchill, Manitoba (magnetic midnight at 6.6 UT). At Dawson, the waves were observed approximately from 00:45 to 04:10 UT (14.4 to 17.8 MLT). At Fort Churchill, waves were observed approximately from 00:00 to 03:10 UT (17.4 to 20.8 MLT). Data from Ministik Lake and Pinawa, located at lower latitude than Dawson and Fort Churchill, show the same basic signature as those sites.

Plots in the second and third panels are from Finland and Russia, both of which show weaker signatures but that are consistent with observations from Canadian Array for Realtime Investigations of Magnetic Activity. Note that all of the Finnish stations (from $L = 5.9$ down to 4.5) observed very similar spectra, though are not shown here.

In the Southern Hemisphere, the induction coil magnetometer at Halley Station (magnetic midnight at 2.7 UT) shows waves occurring from approximately 02:00 to 04:30 UT, or across a region from 23.3 to 01.26 MLT. Again, the bursts of wave power are nearly simultaneous (in universal time) with those in the Northern Hemisphere. Taken together, these observations imply that EMIC waves were excited more or less simultaneously over a broad region, extending from near noon MLT (at Magadan), throughout the dusk and midnight regions and extending to dawn MLT (at Sodankylä).

2.2. EMIC Waves Observed in Space

GOES 13 and 15 overlap with the Canadian sites and observe a region from approximately 16 to 22.5 in magnetic local time at geosynchronous orbit, with GOES 13 being the eastern spacecraft. Figure 4 shows spectra from both satellites. The white traces in that figure show the equatorial gyrofrequency for He⁺ and O⁺, based on in situ magnetometer data. Waves at GOES 13 are in both the hydrogen and helium bands, while those at GOES 15 are primarily in the helium band.

In the right panel in that figure, GOES 15 shows EMIC bursts that roughly coincide with observations on the ground, in particular a burst beginning near 02:00 UT, a stronger one centered near 03:00 UT, and a weaker burst at 03:35 UT. In the left panel of the figure, GOES 13 shows weaker wave bursts that coincide with those from GOES 15, as well as a brief but stronger signature centered near 01:20 UT.

Important observations are presented in Figure 5, showing Van Allen Probe “A” data from 00:00 to 06:00 UT. The top panel again shows Sym/H. The black trace in the second panel again shows the OMNI dynamic pressure; the red trace shows the pressure calculated from Van Allen Probe A plasma observations, with a pressure baseline subtracted to show perturbations (the pressure from the previous orbit, in this case, which was undisturbed). The correspondence between these pressure variations (and SYM/H) is clear, supporting the idea that pressure perturbations are directly transmitted from the solar wind to the magnetosphere, even throughout the nightside.

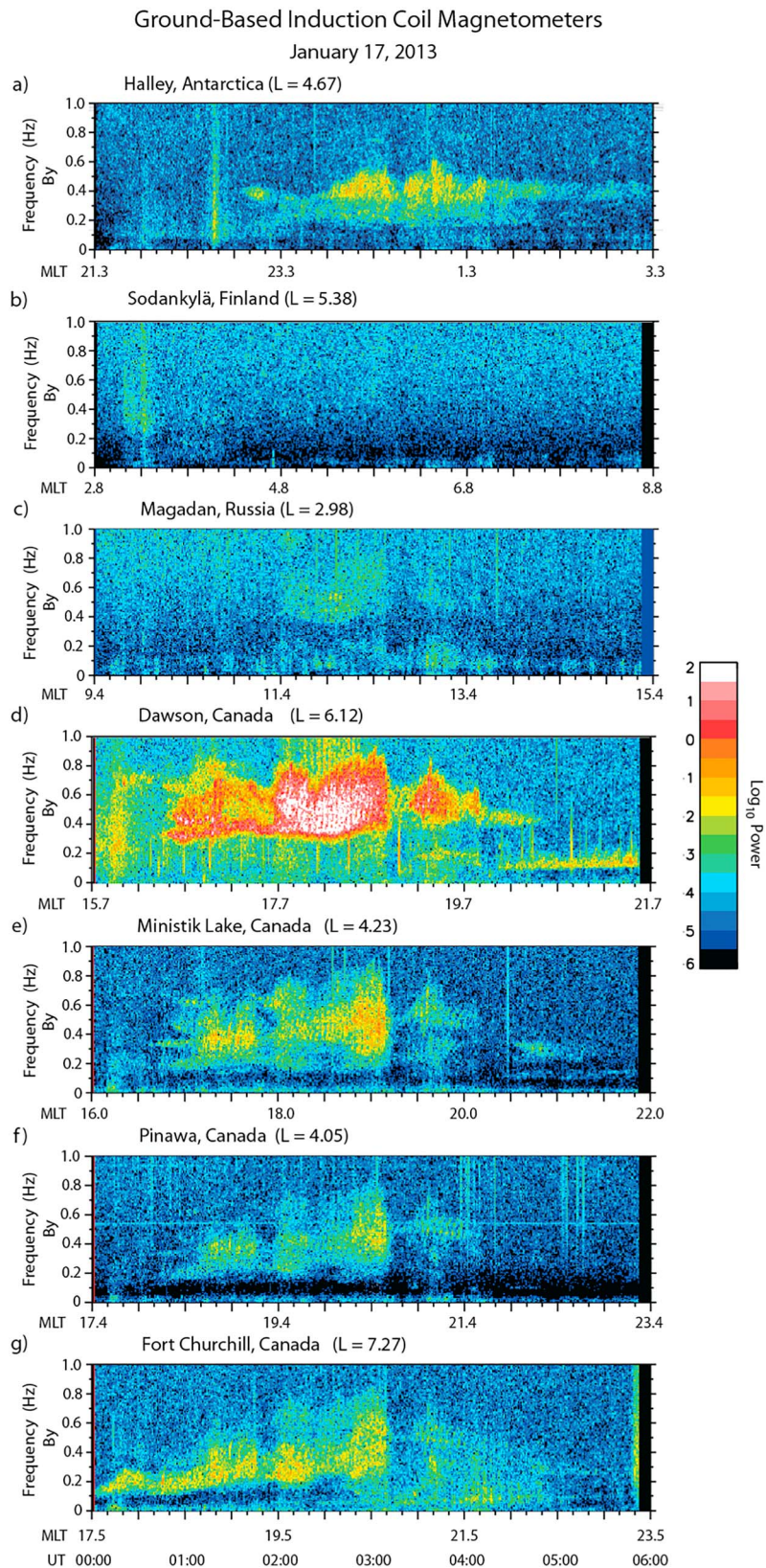


Figure 3. Ground observations from various sites shown in Figure 2, from 00:00 to 06:00 UT, with the order of the plots progressing from east to west in terms of MLT. The simultaneity in electromagnetic ion cyclotron occurrences across all sites is clear in this figure.

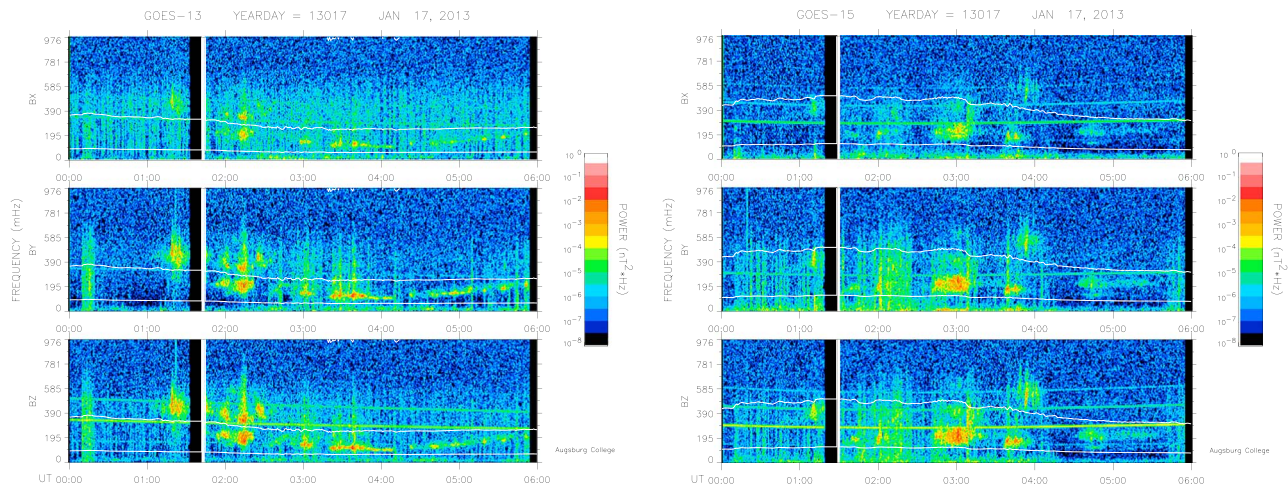


Figure 4. Spectral signatures of electromagnetic ion cyclotron waves from GOES 13 (left) and GOES 15 (right). The white traces in that figure show the equatorial gyrofrequency lines for He⁺ and O⁺, based on in situ magnetometer data. Waves at GOES 13 are in both the hydrogen and helium bands, while those at GOES 15 are primarily in the helium band.

In that figure, pressure is calculated using data from the Helium, Oxygen, Proton, and Electron instrument (Funsten et al., 2013), with density integrated from 100 eV up to the highest energy channel of 50 keV. A full pressure calculation would also include data from the Radiation Belt Storm Probes Ion Composition Experiment instrument (with a range of 20 keV to 1 MeV), but for EMIC waves the energy ranges of the Helium, Oxygen, Proton, and Electron instrument span the most important range for anisotropy estimates.

The bottom panel in that figure also shows low and uniform densities that are characteristic of the spacecraft having exited the plasmopause. The implication is that the wave generation could not have been due to an interaction of the ring current and the plasmopause, as is often thought to be the case.

We note that the broad pressure enhancements extending throughout the period are well correlated with the observed EMIC activity in general, although coincidentally the spacecraft reached apogee at the same time as the peak in pressure. It is near this region in L , in fact, where EMIC waves are generally driven. Still, the broad pressure “peaks” near 02:00 and 03:00 UT are very well correlated with intensifications of EMIC waves observed, for example, at various ground stations (see Figure 3). We conclude from these observations that the solar wind pressure intensifications drove corresponding perturbations within the magnetosphere and subsequently excited the EMIC waves. It is not clear why the waves were excited near the premidnight region.

On Van Allen Probe A, EMIC signatures are observed by the Electric and Magnetic Field Instrument and Integrated Science experiment (Kletzing et al., 2013), occurring from 02:00 until just after 04:00 UT. A reasonable question is whether these bursts of wave activity can be related to specific enhancements in T_{\perp}/T_{\parallel} , the temperature anisotropy. The fourth panel in that figure shows pressure anisotropy, which is a proxy for temperature anisotropy if the density is constant. Again, the bottom panel in the figure shows that this is the case throughout that interval. The lack of correspondence between the small-scale pressure perturbations and EMIC wave generation may imply that the waves were generated away from the region where they are observed.

2.3. Particle Precipitation

Several theoretical studies investigating the dynamics of EMIC waves on the ring current have shown that EMIC waves can scatter protons with tens of kiloelectron volts into the loss cone over time scales of hours (Lyons & Thorne, 1972; Xiao et al., 2011). Observationally, proton precipitation and EMIC waves have been correlated using satellite particle fluxes (Yahnina et al., 2000), the IMAGE-FUV SI12 detecting proton flashes (Popova et al., 2010), and stable aurora red arcs (Cornwall et al., 1971; Lundblad & Soraas, 1978). The EMIC waves here are observed both by spacecraft as well as on the ground when close in magnetic local time to the proton precipitation.

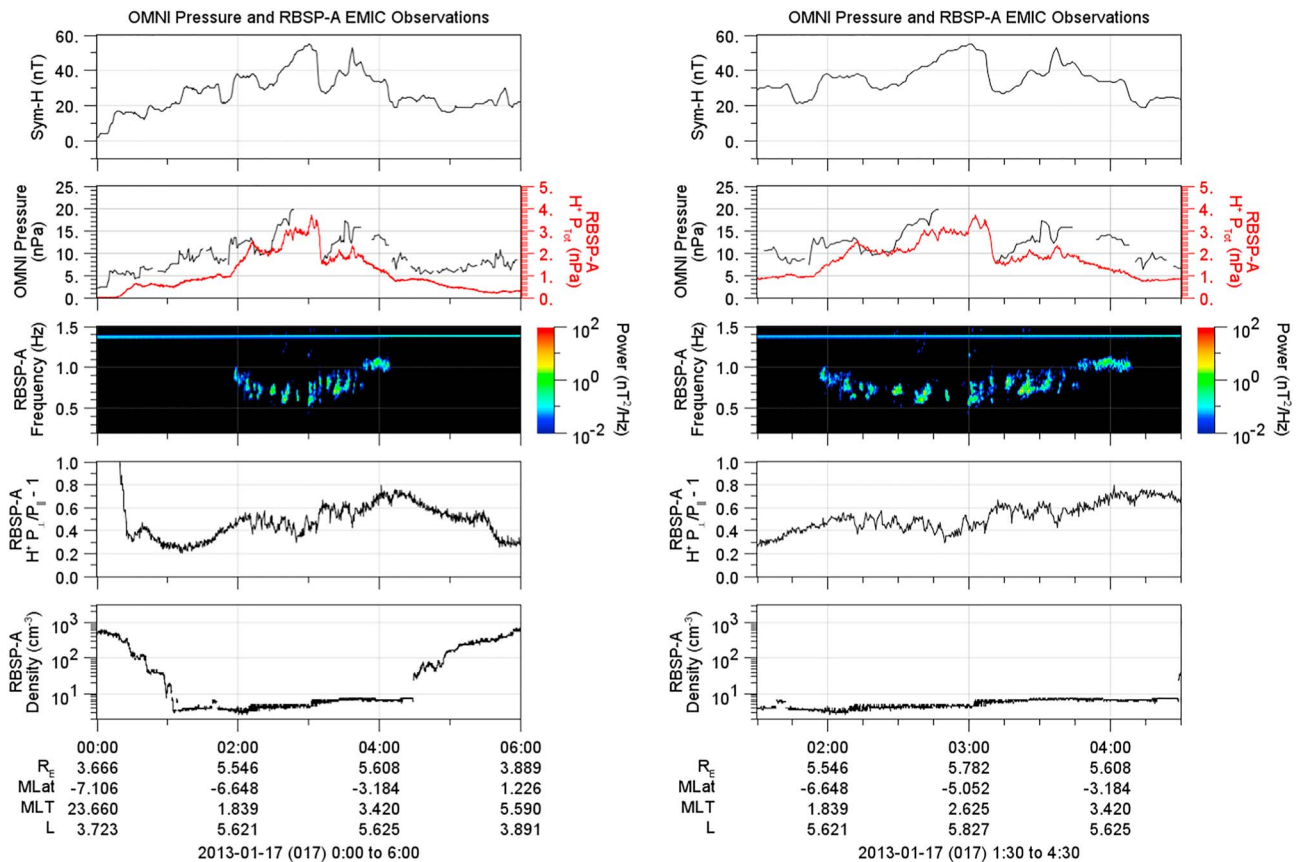


Figure 5. Data from Van Allen Probe A. In each panel, we show the SYM/H index, the OMNI solar wind pressure in black and the pressure at the satellite location in red, calculated from the measured fluxes. The third panel shows magnetic field dynamic spectra, with electromagnetic ion cyclotron (EMIC) wave bursts throughout the higher L shells. The fourth panel shows the calculated pressure anisotropy, which is a proxy for the temperature anisotropy if the density is constant, which is shown to be the case in the bottom panel. The plot on the left shows the entire 00:00–06:00 UT interval; the plot on the right provides a closer look, intended to show that although a one-to-one correspondence does not exist between EMIC occurrences and fluctuations in the temperature anisotropy, the temporal variations are similar.

In a study using ground-based observations of EMIC waves and correlating these with low altitude satellite observations of precipitating protons in the 30- to 80-keV range, Engebretson et al. (2008) found that waves were associated with precipitation during storm recovery phases and, conversely, the lack of waves during onset and main phase corresponded to an absence of precipitation.

EMIC waves can also resonantly interact with radiation belt electrons. This has been shown to be true for electrons with energies greater than ~ 1 MeV (Lyons & Thorne, 1972) although Meredith et al. (2003), using quasi-linear theory, showed it is possible to get sub-megaelectronvolt interaction energies (also see Chen et al., 2016, and Lee et al., 2018). Theoretical calculations suggest that intense (1–10 nT) storm time EMIC waves can rapidly scatter radiation belt electrons, a process that may significantly contribute to outer electron belt depletion, often seen at the onset of geomagnetic storms (Summers & Thorne, 2003).

2.3.1. POES Observations

Here we are building on the work of Sandanger et al. (2007) and Carson et al. (2013), who used the fact that both ions and relativistic electrons can be precipitated by EMIC waves to develop a proxy for EMIC-driven precipitation. The technique examines precipitation signatures in POES MEPED data and assumes that the presence of short-lived precipitation spikes in the POES 30- to 80-keV proton and >800 -keV electron loss cone is indicative of EMIC-driven precipitation. This has been developed into an automatic algorithm (described by Carson et al., 2013). Validation of this technique is provided via a conjunction, where a POES-reported precipitation trigger occurred within seconds of Van Allen Probe A observing the start of an EMIC wave event, with the POES NOAA-15 satellite located very near the base of the field line that passed through Van Allen Probe A (Rodger et al., 2015).

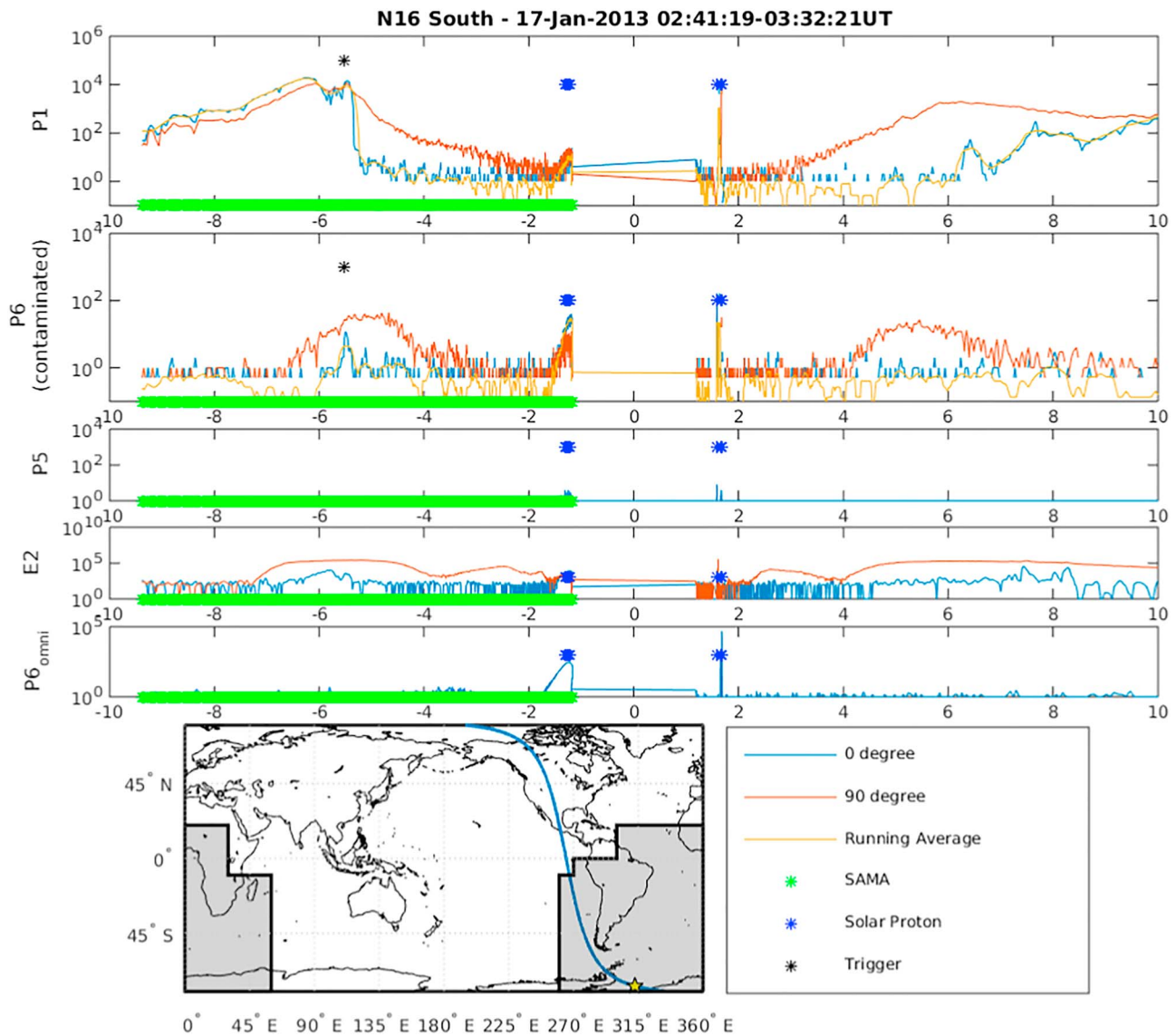


Figure 6. NOAA POES data. The top panel (P1) shows the 30- to 80-keV proton data, with 0° pitch angle data (blue), 90° data (brown), and a running average of the 0° data (amber). The second panel (P6) shows relativistic electron precipitation. The horizontal axis gives the L shell of the POES spacecraft. The black stars in both of these panels indicate the “trigger” time, where the peak was manually detected in P6. The green line at the bottom is actually a succession of green stars and indicates the spacecraft was passing through the zone where the particle fluxes are affected by the South American Magnetic Anomaly, shown by the gray shaded box in the map at the bottom. The star at the bottom right of the map is the location of the POES satellite footprint at the time of the event trigger, which was in fact quite close to Halley.

Recent work combining the POES algorithm-detected EMIC precipitation and ground-based magnetometer observations has also lent strong support to the validity of the technique (Hendry et al., 2016). The automatic detection technique necessarily underestimates the role of EMIC waves in the scattering process, since there may be cases where only ions are scattered, or when the scattered electrons are outside the effective energy range of the POES spacecraft. We also note that there are some cases where proton precipitation is not observed because the scattered protons are out of the energy range of the POES measurements (Wang et al., 2014; Yuan et al., 2018).

POES satellite coverage in terms of MLT for this event is fairly good. In general, the POES spacecraft coverage is not uniform, with three of the spacecraft being in the same magnetic local time plane and with no coverage at 0, 6, 12, or 18 MLT (see Engebretson et al., 2018). Still, during the interval from 00:00 to 06:00 UT for this event, six POES spacecraft completed a total of 21 (~3.5 per s/c) orbits to provide coverage at several magnetic local times.

Table 1
Proton Precipitation Observed by NOAA Satellites, Ordered by the Universal Time of the Observations

	Time	<i>L</i> shell	MLT	Latitude	Longitude
NOAA-19	00:10:46	7.0	18.4	-77.97	235.69
NOAA-15	01:35:58	6.1	13.8	66.13	209.46
NOAA-19	01:56:08	7.5	16.9	-67.85	193.47
NOAA-15	02:27:52	5.6	0.6	-72.04	14.88
NOAA-17	03:06:52	7.9	15.4	67.88	216.75
NOAA-17	03:07:18	8.7	15.2	69.23	215.10
NOAA-16	03:23:48	6.4	18.1	59.76	246.09
NOAA-16	03:24:36	7.7	17.9	62.30	244.15
NOAA-16	03:37:10	6.5	9.9	71.50	104.53
NOAA-19	03:40:52	7.4	15.4	-59.27	162.05
NOAA-18	04:01:10	6.7	17.6	-62.93	181.77
NOAA-16	04:16:38	7.1	4.5	-66.43	52.81
NOAA-19	04:30:36	6.1	3.3	64.42	332.92
NOAA-18	04:49:58	8.2	5.5	70.74	358.98
METOP-02	05:24:54	6.8	5.6	-67.44	46.72

The POES autodetection algorithm searches the POES MEPED data for approximately simultaneous sudden, short-lived enhancements in the P1 (52-keV differential proton flux channel) and P6 (larger than about 800-keV electron channel) 0° (loss cone) detectors. In the algorithm, “simultaneity” is taken to be a P6 peak (or “trigger”) occurring within $\pm \sim 8$ s of a P1 peak. A detailed description of this algorithm is given in Carson et al. (2013).

With the P6 (electron contaminated) channel, there is usually little difficulty in detecting the precipitation spikes, as there is generally little flux activity in the channel (outside of solar proton events, which can be identified from the P5 channel). The P1 channel, however, typically has large levels of flux activity, which can make differentiating between EMIC-related precipitation spikes and general flux “noise” in the channel difficult, or impossible. The algorithm takes a safe approach and requires a very clear, large spike in the P1 channel, at the expense of missing some events. Lowering this threshold would risk more false positives, which is to be avoided.

POES data for the interval from 00:00-06:00 UT on 17 January 2013 were examined using this algorithm, with no simultaneous electron and ion precipitation events being detected. A manual examination of the data identified a single event that was missed by the algorithm due to the P1 noise issues explained above. This event, as recorded by NOAA-16 between 02:41:19 and 03:32:21 UT, is presented in Figure 6, where the top panel (P1) shows the 30- 80-keV proton data, with 0° pitch angle data (blue), 90° data (brown), and a running average of the 0° data (amber). The second panel (P6) shows relativistic electron precipitation. The horizontal axis gives the *L* shell of the POES spacecraft. The black stars in both of these panels indicate the “trigger” time, where the peak was manually detected in P6. The green line at the bottom is actually a succession of green stars and indicates the spacecraft was passing through the zone where the particle fluxes are affected by the South American Magnetic Anomaly, shown by the gray shaded box in the map at the bottom. The star at the bottom right of the map is the location of the POES satellite footprint at the time of the event trigger, which was in fact quite close to Halley.

The Carson et al. (2013) algorithm was run for the same period, with the requirement for a simultaneous peak in P6 removed (i.e., only peaks in P1 were considered). The resulting list of proton precipitation events is listed by their occurrence in universal time in Table 1, as well as their *L* shell and MLT positions. While there is no direct correspondence between these events and the EMIC waves described above, the preponderance of both throughout the interval implies a strong correlation between them. Note that 9 of the 16 events occurred in the range of 13.8 to 18.4 MLT and that these appeared in the earlier part of the window. Five of the events, which occurred later in the window, were located between 3.3 and 9.9 MLT. The lack of POES satellite

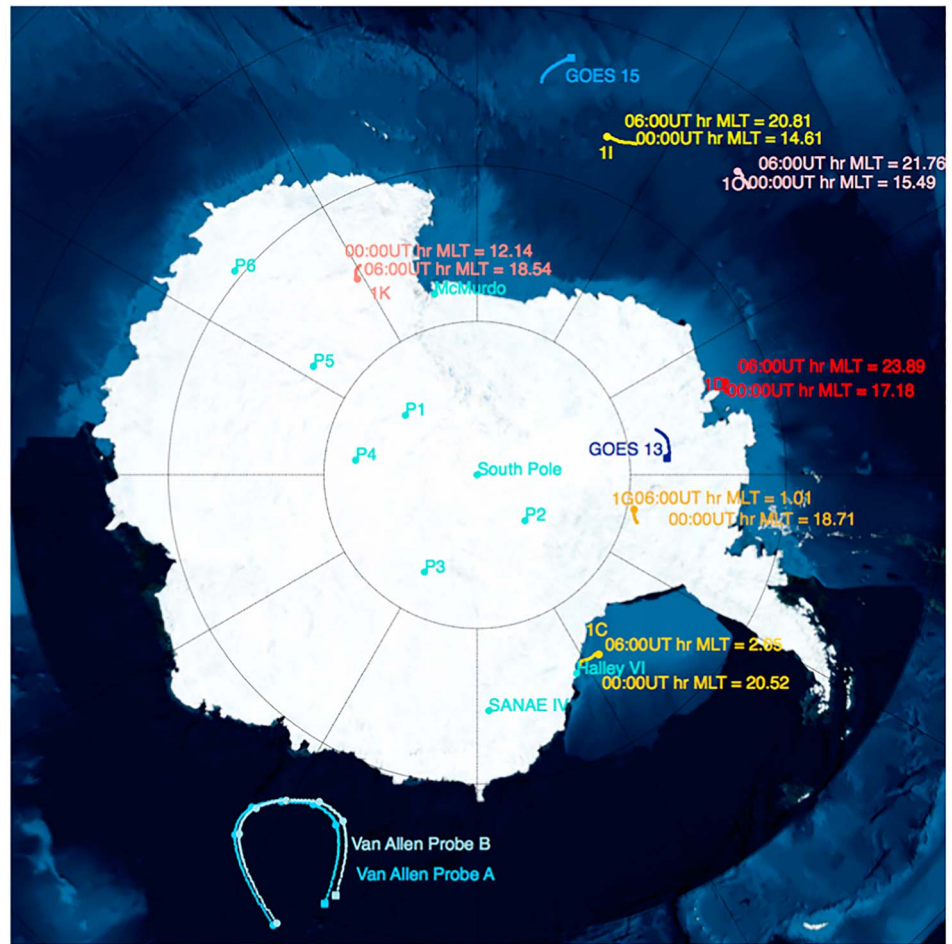


Figure 7. Map of Antarctica, showing the locations of the Balloon Array for RBSP Relativistic Electron Losses balloons (1C, 1D, 1G, 1I, 1K, and 1O), Halley Station, the footprints of GOES 13 and 15, and the footprint of the Van Allen Probe A satellites.

coverage in the midnight MLT region for this event leaves somewhat of an untold story in the interpretation of these data.

The general lack of electron precipitation signatures in the POES data shows that, in spite of the widespread EMIC activity, relativistic electron precipitation appears to have been absent or confined spatially. This is discussed further in the next section. Proton precipitation was more evident, though relating these data directly to the EMIC observations may not be reasonable, other than to see that both were persistent and widespread throughout the interval.

2.3.2. Balloon Array for RBSP Relativistic Electron Losses Observations

During the time of this event, the BARREL (Balloon Array for RBSP Relativistic Electron Losses) campaign was operating in its first season. During this campaign, a total of 20 small (~20 kg) balloon payloads were launched to an altitude of 30–35 km with the goal of maintaining an array of five to eight operational payloads at any given time, spreading across *L* shells from ~3 to 8. Each balloon carried a NaI scintillator to measure bremsstrahlung X-rays produced by precipitating energetic electrons as they collide with neutrals in Earth's atmosphere. The energies of the X-rays provide a measure of the relativistic precipitating electron energies and provide a measure of relativistic electron precipitation from 20 keV to 10 MeV.

Three different data products are derived from the instruments are provided, including fast spectra, medium spectra, and slow spectra, all with trade-offs in sample rates and energy resolution. The data provided in this paper include slow spectra, with energies from 25 keV to 10 MeV in 256 energy channels and a time resolution of 32 s (Woodger et al., 2015). Fast spectra is also used, which has four energy channels (<180 keV, 180–550 keV, 550–840 keV, and 840 keV to 1.5 MeV), at a time resolution of 50 ms.

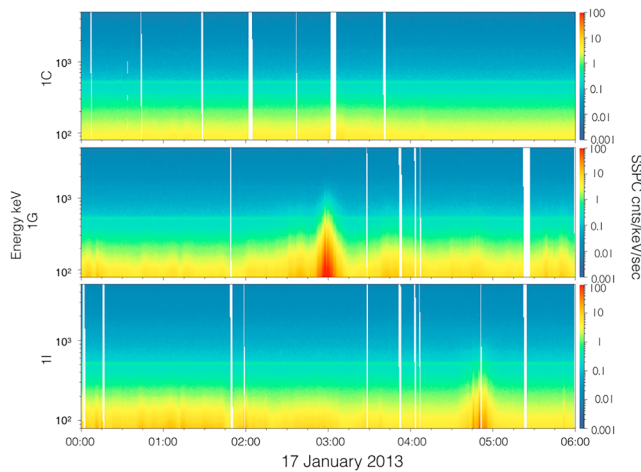


Figure 8. Observations of X-ray counts by each balloon used in this study, from 00:00 to 06:00 UT. The data presented are “Slow Spectra” (SSPC), which includes energies from 25 keV to 10 MeV in 256 energy channels with a time resolution of 32 s. See text for description of precipitation signatures.

Figure 7 shows the Antarctic continent, with the locations of various balloons, as well as Halley Station and the magnetic footprints of GOES-13, GOES-15, and the Van Allen Probes. The GOES satellites are geosynchronous, so their footprints remain quasi-stationary. X-ray signatures were detected by 1G and 1I at various times during the 00:00–06:00 UT interval, with the most intense signatures near geosynchronous orbit (at balloon 1G). Balloon 1C shows a data gap during the event detected by 1G, which may have prevented a similar observation. Balloons 1D, 1K, and 1O did not detect any notable activity.

Data from the balloons are shown in Figure 8. All three balloons mapped reasonably closely to the magnetic locations of GOES 15, GOES 13, and Halley. Again, the widespread observations of EMIC waves suggest that these waves were more or less being generated globally, though perhaps not uniformly. Weak X-ray fluxes were observed in the lowest energy channels (e.g., 100–200 keV) by the 1G and 1I balloons from the very beginning of this interval and persisted more or less throughout the duration. By far, the most intense count rates are detected by the 1G balloon, peaking near 02:58 UT, with a total duration of ~15 min. The peak of the magnetospheric compression occurs right around this time, which also corresponds to the peak in the SYM-H index, again suggesting that the waves and the associated precipitation were driven by compressions of the magnetosphere (see Figure 1).

Li et al. (2014) provide a thorough analysis of the BARREL 1G signatures, modeling the pitch angle scattering of electrons by EMIC waves as observed by GOES 13 during this time and then also modeling the expected BARREL signatures of X-rays from this precipitation. They conclude that the X-ray signatures indicate the precipitation of electrons having energies with highest fluxes near 1.2 MeV and that these electrons were

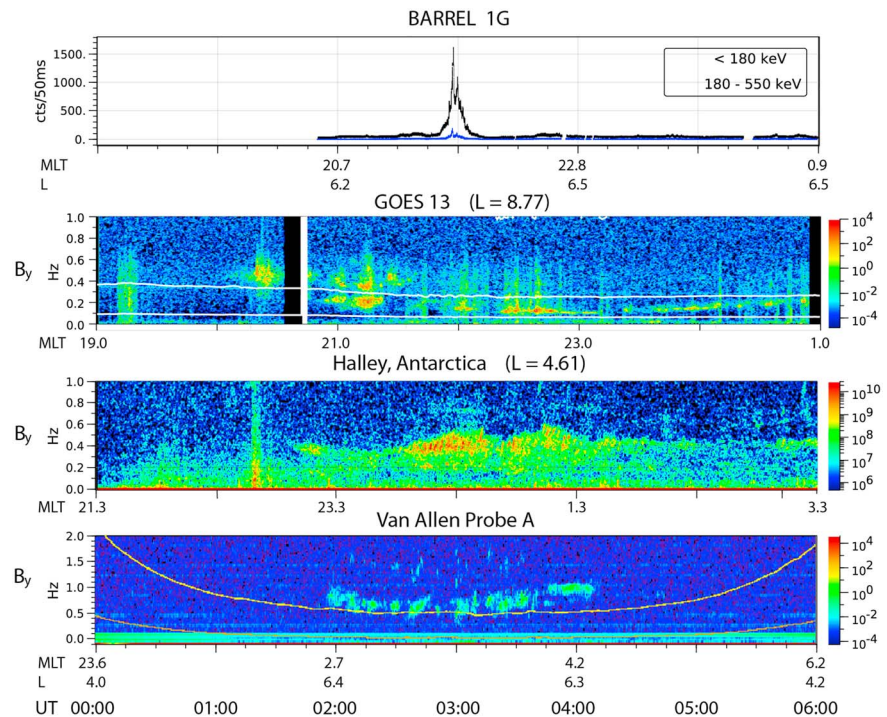


Figure 9. Composite figure showing simultaneous occurrences of X-ray bursts observed by the 1G balloon in the first panel. Other panels show electromagnetic ion cyclotron signatures from GOES 13, at Halley Station and by Van Allen Probe A. The equatorial gyrofrequency lines for He⁺ and O⁺ are plotted in white. BARREL = Balloon Array for RBSP Relativistic Electron Losses.

scattered by EMIC waves. In addition, Shprits et al. (2016) also attributed the loss of 4.2-MeV electrons to EMIC waves several hours later on the same day.

This burst occurs when EMIC waves are observed by GOES 13, at Halley Station and by the Van Allen Probe A satellite, as shown in Figure 9. At the time of this event, these observing platforms bracketed the 1G and 1C balloons in magnetic local time. While the 1G observed a strong signature, the 1C balloon recorded no enhancement at all. A second burst of precipitation was recorded by the 1I balloon from 04:40 to 05:00 UT. This burst coincides with the onset of lower-frequency EMIC waves at Ministik Lake, Dawson, and GOES 15. It appears that the electron precipitation was also related to the EMIC waves, given the relatively close proximity of all of these observing platforms.

While the general correlations would suggest that the precipitation must have been driven by the EMIC waves, which were clearly very widespread during this time, the lack of signatures at 1C and the isolated bursts at 1G and 1I suggest that the process may be intermittent or patchy. One hypothesis would be that the appropriate electron populations were simply absent from the region where waves developed and thus relativistic electrons were not available to be scattered by the waves.

On the other hand, Woodger et al. (2018) studied this same event and emphasize that although EMIC waves may be widespread; their ability to scatter energetic electrons depends on the value of the local magnetic field strength. Building on the work of Li et al. (2014), they use a quasi-linear diffusion model to study observations at the 1I balloon and show that as the balloon drifts in local time to regions mapping to lower equatorial magnetic field strength, precipitating electrons have fluxes that are peaked at lower energy.

For this particular time period, the radiation belts were largely depleted of higher-energy relativistic electrons, which means only the waves that can effectively scatter lower-energy electrons will produce measurable precipitation. Woodger et al. (2018) explain that these conditions were met only when the 1I balloon drifted to later magnetic local times.

2.3.3. Van Allen Probe Magnetic Electron Ion Spectrometer observations

Figure 10 shows data from the Magnetic Electron Ion Spectrometer sensor of the RBSP-ECT instrument suite (Spence et al., 2013), which uses magnetic focusing and pulse height analysis to provide energetic electron measurements over the energy range of 30 keV to 4 MeV (Blake et al., 2013). The plot shows electron distributions as a function of pitch angle from 80 keV to nearly ~ 1 MeV, plotted versus time.

As shown on the right-hand side of Figure 5, EMIC waves occurred in a bursty fashion in the vicinity of the satellite, more or less continuously throughout its apogee pass. During this period, which extends from 01:56 to 04:09 UT, the spacecraft drifted from $L = 5.6$, out to its apogee of $L = 6.2$ (not shown), and then back to $L = 5.6$. An obvious question is whether these waves contribute to the modification of electron distributions and/or to the scattering into the loss cone.

The Magnetic Electron Ion Spectrometer data show typical butterfly distributions throughout the interval, that is, reductions in differential fluxes near 90° pitch angles. This narrowing of pitch angles to become more field aligned can be seen faintly in all channels, but much more strongly in the 730-keV and 1.0-MeV channels. The formation of butterfly distributions has been shown to result from drift shell splitting, a process that drives lower pitch-angle particles to lower L shells and higher pitch-angle particles to higher L shells as they drift in a nondipolar field. Note that there is mounting evidence that butterfly distributions might also be generated through magnetosonic waves (Li et al., 2016; Xiao et al., 2015).

Sibeck et al. (1987) examined Active Magnetospheric Particle Tracer Explorer; Charge Composition Explorer (AMPTE CCE) data and showed that substorm-injected particles with 90° pitch angles drifting around to the dayside can undergo drift shell splitting, with higher-energy electrons drifting nearly to the open-closed boundary. This effect was confirmed in a case study by Lessard et al. (2009), who showed that substorm-injected electrons precipitated to the ground in this region. Min et al. (2010) proposed that chorus waves, associated with the drift shell splitting, were likely responsible for ultimately scattering the electrons into the loss cone for that event.

Sibeck et al. (1987) also pointed out that magnetospheric compressions from storms can likewise intensify drift shell splitting due to the increased distortion of Earth's field, an idea that had previously been described by Wilken et al. (1986). These authors used data from geosynchronous satellites to show that an SSC-driven nonadiabatic compression intensified the drift shell splitting and resulted in field-aligned populations near the midnight region.

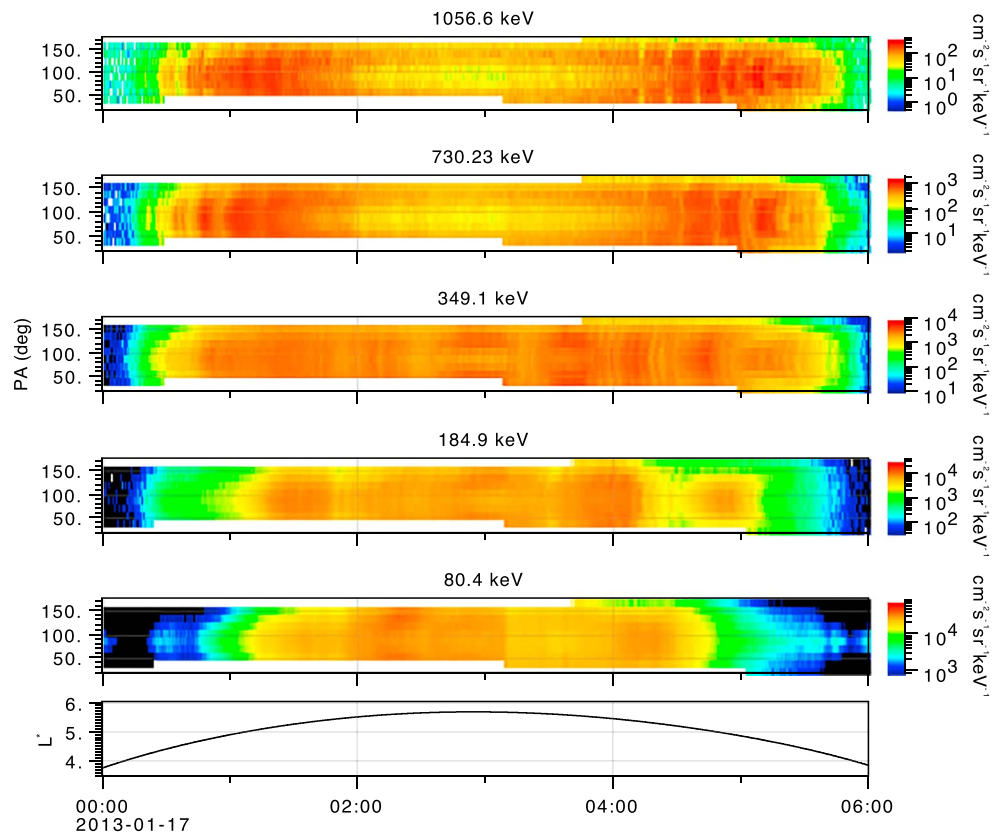


Figure 10. Magnetic Electron Ion Spectrometer data from the Van Allen Probe A satellite. The plot shows electron pitch angle distribution functions from 80-keV to ~1-MeV electrons, plotted versus time. As shown on the right-hand side of Figure 5, electromagnetic ion cyclotron waves occurred in a bursty fashion in the vicinity of the satellite, more or less continuously throughout its apogee pass. During this period, which extends from 01:56 to 04:09 UT, the spacecraft moved in its orbit from $L = 5.6$, out to its apogee of $L = 6.2$ (not shown) and then back to $L = 5.6$.

Recently, Xiao et al. (2015) reported Van Allen Probe observations of a butterfly distribution of relativistic electrons well inside geostationary orbit during a magnetic storm (at lower L shells than where such populations are normally observed). Based on their simulation results, they conclude that the distributions were driven by chorus and magnetosonic waves and emphasize the possibility that waves may contribute to the formation of butterfly distributions. Rodger et al. (2015) also noted butterfly distributions in Van Allen Probe observations, spanning wide energy ranges and coincident with the onset of EMIC waves.

The butterfly distributions in Figure 10 are also well within geosynchronous orbit and occurred concurrently with EMIC wave activity in the vicinity. On the other hand, the patchy character of EMIC wave occurrences contrasts with the smooth evolution of the butterfly distributions as the spacecraft crosses L shells, perhaps suggesting that the waves had no observable effect on the particles.

Finally, the question of whether energetic electrons precipitated into the loss cone in this MLT is best answered by the examination of POES MEPED data, as described above. There were approximately five close encounters during this interval, with NOAA-17 crossing the Van Allen Probe A orbit near 03:57 UT. A closer look at the MEPED data was completed but showed no evidence of strong precipitation, nor anything that looks like the expected EMIC precipitation signature.

3. Summary and Conclusions

In this paper, we present data from a magnetospheric compression that occurred on 17 January 2013. Several ground-, balloon- and space-based observing platforms contribute data to this study, which focuses (1) on the widespread generation of EMIC waves during the event and (2) ion and electron precipitation during the event. The event was unusual in that the IMF was northward for the entire period that was examined,

aside from a brief and weak excursion. Still, SYM/H reached a maximum value of 55 nT, and radiation belt precipitation was observed. We are led to the following conclusions:

1. With B_z remaining positive for the entire time, reconnection at the dayside subsolar magnetopause was absent or weak, at best. As a result, pressure fluctuations in the solar wind appear to have been directly transferred to the magnetosphere and then propagated throughout the magnetosphere. This conclusion is supported by the strong correlations between temporal variations in the solar wind dynamic pressure, the SYM/H index, and pressure variations recorded by Van Allen Probe A. We also conclude that the positive excursion in SYM/H resulted from the intensification of magnetopause currents and, perhaps, had little or nothing to do with the ring current.
2. The global pressure perturbation appears to have been responsible for the temperature anisotropy needed to generate EMIC waves. Waves with very similar spectral signatures and temporal variations were recorded clearly throughout the dusk to postmidnight sector, with weaker signatures observed near dawn and also near noon. The intensifications of these waves closely tracked SYM/H and also the solar wind pressure, again pointing to the pressure perturbation as the driver for these waves.
3. Electron precipitation was recorded by the BARREL balloons, although it did not have the same widespread signatures as the waves. In fact, the electron precipitation appears to have been quite patchy in character, perhaps corresponding to the presence of localized resonance conditions as explained by Woodger et al. (2018). Observations from Van Allen Probe A (postmidnight) showed clear butterfly distributions, and it may be possible that the EMIC waves contributed to the development of these distribution functions, though no precipitating electrons were recorded by a NOAA satellite that flew very close to the footprint of Van Allen Probe A. Ion precipitation was also recorded by the fleet of POES satellites (which include the NOAA satellites), though tended to be confined to the dawn-dusk meridians.

Acknowledgments

We gratefully acknowledge helpful discussions with V. Jordanova during this effort. We thank Kazuo Shiokawa of Nagoya University for provision of Magadan search coil data and Tero Raita of Sodankyla Geophysical Observatory for provision of Sodankyla search coil data. We also thank I. R. Mann, D. K. Milling, and the rest of the CARISMA team for data. CARISMA is operated by the University of Alberta, funded by the Canadian Space Agency. We also acknowledge the gracious support provided at Halley Station by the British Antarctic Survey. Support for this work was provided at UNH by NSF awards PLR-1341677 and ANT-1141987. Support at Augsburg College was provided by NSF awards PLR-1341493 and ANT-1142045. A. J. H. was supported by NASA under Grant NNX15AF66G. The research by C. J. R. and A. T. H. leading to these results was supported by the European Community Seventh Framework Programme ([FP7/2007013]) under Grant 263218. Support for NASA Van Allen Probes efforts was provided through Grant NAS5-01072. Data used in this paper are available at NOAA National Geophysical Data Center (NGDC – POES MEPED data) and the University of Alberta CARISMA data repository (magnetometer data at Canadian sites). Other data used in this study are available at space.augsburg.edu/searchcoilrequest. Links to the dynamic spectrograms are available through the Virtual Waves Observatory (VWO) at NASA/Goddard Space Flight Center, and 0.5-second cadence digital data from Halley and South Pole, Antarctica, from 2004 to 2007 are archived at the Virtual Magnetospheric Observatory (VMO) at UCLA.

References

- Allen, R. C., Zhang, J.-C., Kistler, L. M., Spence, H. E., Lin, R.-L., Klecker, B., et al. (2015). A statistical study of EMIC waves observed by Cluster: 1. Wave properties. *Journal of Geophysical Research: Space Physics*, *120*, 5574–5592. <https://doi.org/10.1002/2015JA021333>
- Anderson, B. J., Erlanson, R. E., & Zanetti, L. J. (1992). A statistical study of Pc 1–2 magnetic pulsations in the equatorial magnetosphere, 1, Equatorial occurrence distributions. *Journal of Geophysical Research*, *97*, 3075–3101.
- Anderson, B. J., & Hamilton, D. C. (1993). Electromagnetic ion cyclotron waves stimulated by modest magnetospheric compressions. *Journal of Geophysical Research*, *98*, 11,369–11,382. <https://doi.org/10.1029/93JA006605>
- Arnoldy, R. L., Engebretson, M. J., Denton, R. E., Posch, J. L., Lessard, M. R., Maynard, N. C., et al. (2005). Pc 1 waves and associated unstable distributions of magnetospheric protons observed during a solar wind pressure pulse. *Journal of Geophysical Research*, *110*, A07229. <https://doi.org/10.1029/2005JA011041>
- Blake, J. B., Carranza, P. A., Claudepierre, S. G., Clemmons, J. H., Crain, W. R., Dotan, Y., et al. (2013). The Magnetic Electron Ion Spectrometer (MagEIS) Instruments aboard the Radiation Belt Storm Probes (RBSP) spacecraft. *Space Science Reviews*, *179*, 383–421. <https://doi.org/10.1007/s11214-013-9991-8>
- Blum, L. W., Halford, A., Millan, R., Bonnell, J. W., Goldstein, J., Usanova, M., et al. (2015). Observations of coincident EMIC wave activity and duskside energetic electron precipitation on 18–19 January 2013. *Geophysical Research Letters*, *42*, 5727–5735. <https://doi.org/10.1002/2015GL065245>
- Bräysy, T., Mursula, K., & Marklund, G. (1998). Ion cyclotron waves during a great magnetic storm observed by Freja double-probe electric field instrument. *Journal of Geophysical Research*, *103*, 4145–4156. <https://doi.org/10.1029/97JA02820>
- Burton, R. K., McPherron, R. L., & Russell, C. T. (1975). An empirical relationship between interplanetary conditions and Dst. *Journal of Geophysical Research*, *80*(31), 4204–4214. <https://doi.org/10.1029/JA080i031p04204>
- Carson, B. R., Rodger, C. J., & Clilverd, M. A. (2013). POES satellite observations of EMIC-wave driven relativistic electron precipitation during 1998–2010. *Journal of Geophysical Research: Space Physics*, *118*, 232–243. <https://doi.org/10.1029/2012JA017998>
- Chen, L., Thorne, R. M., Bortnik, J., & Zhang, X.-J. (2016). Nonresonant interactions of electromagnetic ion cyclotron waves with relativistic electrons. *Journal of Geophysical Research: Space Physics*, *121*, 9913–9925. <https://doi.org/10.1002/2016JA022813>
- Cho, J.-H., Lee, D.-Y., Noh, S.-J., Kim, H., Choi, C. R., Lee, J., & Hwang, J. (2017). Spatial dependence of electromagnetic ion cyclotron waves triggered by solar wind dynamic pressure enhancements. *Journal of Geophysical Research: Space Physics*, *122*, 5502–5518. <https://doi.org/10.1002/2016JA023827>
- Cornwall, J. M., Coroniti, F. V., & Thorne, R. M. (1970). Turbulent loss of ring current protons. *Journal of Geophysical Research*, *75*, 4699. <https://doi.org/10.1029/JA075i025p04699>
- Cornwall, J. M., Hilton, H. H., & Mizera, P. F. (1971). Observations of precipitating protons in the energy range $2.5 \text{ keV} \leq E \leq 200 \text{ keV}$. *Journal of Geophysical Research*, *76*, 5220–5234.
- Engebretson, M. J., Lessard, M. R., Bortnik, J., Green, J. C., Horne, R. B., Detrick, D. L., et al. (2008). Pc1–Pc2 waves and energetic particle precipitation during and after magnetic storms: Superposed epoch analysis and case studies. *Journal of Geophysical Research*, *113*, A01211. <https://doi.org/10.1029/2007JA012362>
- Engebretson, M. J., Posch, J. L., Capman, N. S. S., Campuzano, N. G., Belik, P., Allen, R. C., et al. (2018). MMS, Van Allen Probes, GOES 13, and ground based magnetometer observations of EMIC wave events before, during, and after a modest interplanetary shock. *Journal of Geophysical Research: Space Physics*, *123*, 8331–8357. <https://doi.org/10.1029/2018JA025984>
- Engebretson, M. J., Posch, J. L., Wygant, J. R., Kletzing, C. A., Lessard, M. R., Huang, C.-L., et al. (2015). Van Allen probes, NOAA, GOES, and ground observations of an intense EMIC wave event extending over 12 h in magnetic local time. *Journal of Geophysical Research: Space Physics*, *120*, 5465–5488. <https://doi.org/10.1002/2015JA021227>

- Francia, P., Lepidi, S., Villante, U., Di Giuseppe, P., & Lazarus, A. J. (1999). Geomagnetic response at low latitude to continuous solar wind pressure variations during northward interplanetary magnetic field. *Journal of Geophysical Research*, *104*(A9), 19,923–19,930. <https://doi.org/10.1029/1999JA900229>
- Fraser, B. J. (1975). Ionospheric duct propagation and Pc 1 pulsation sources. *Journal of Geophysical Research*, *80*, 2790–2796. <https://doi.org/10.1029/JA080i019p02790>
- Fraser, B. J., & Nguyen, T. S. (2001). Is the plasmopause a preferred source region of electromagnetic ion cyclotron waves in the magnetosphere? *Journal of Atmospheric and Solar-Terrestrial Physics*, *63*, 1225–1247. [https://doi.org/10.1016/S1364-6826\(00\)00225-X](https://doi.org/10.1016/S1364-6826(00)00225-X)
- Funsten, H. O., Skoug, R. M., Guthrie, A. A., MacDonald, E. A., Baldonado, J. R., Harper, R. W., et al. (2013). Helium, Oxygen, Proton, and Electron (HOPE) Mass Spectrometer for the Radiation Belt Storm Probes Mission. *Space Science Reviews*, *179*, 423–484. <https://doi.org/10.1007/s11214-013-9968-7>
- Greifinger, P. (1972). Ionospheric propagation of oblique hydromagnetic plane waves at micropulsation frequencies. *Journal of Geophysical Research*, *77*, 2377–2391.
- Halford, A. J., Fraser, B. J., & Morley, S. K. (2010). EMIC wave activity during geomagnetic storm and nonstorm periods: CRRES results. *Journal of Geophysical Research*, *115*, A12248. <https://doi.org/10.1029/2010JA015716>
- Halford, A. J., Fraser, B. J., & Morley, S. K. (2015). EMIC waves and plasmaspheric and plume density: CRRES results. *Journal of Geophysical Research: Space Physics*, *120*, 1974–1992. <https://doi.org/10.1002/2014JA020338>
- Hendry, A. T., Rodger, C. J., & Clilverd, M. A. (2017). Evidence of sub-MeV EMIC-driven electron precipitation. *Geophysical Research Letters*, *44*, 1210–1218. <https://doi.org/10.1002/2016GL071807>
- Hendry, A. T., Rodger, C. J., Clilverd, M. A., Engebretson, M. J., Mann, I. R., Lessard, M. R., et al. (2016). Confirmation of EMIC wave-driven relativistic electron precipitation. *Journal of Geophysical Research: Space Physics*, *121*, 5366–5383. <https://doi.org/10.1002/2015JA022224>
- Horne, R. B., & Thorne, R. M. (1993). On the preferred source location for the convective amplification of ion cyclotron waves. *Journal of Geophysical Research*, *98*, 9233–9247. <https://doi.org/10.1029/92JA02972>
- Jordanova, V. K., Spasojevic, M., & Thomsen, M. F. (2007). Modeling the electromagnetic ion cyclotron wave-induced formation of detached subauroral proton arcs. *Journal of Geophysical Research*, *112*, A08209. <https://doi.org/10.1029/2006JA012215>
- Kepko, L., & Spence, H. E. (2003). Observations of discrete, global magnetospheric oscillations directly driven by solar wind density variations. *Journal of Geophysical Research*, *108*(A6), 1257. <https://doi.org/10.1029/2002JA009676>
- Kim, H., Lessard, M. R., Engebretson, M. J., & Young, M. A. (2011). Statistical study of Pc1-2 wave propagation characteristics in the high-latitude ionospheric waveguide. *Journal of Geophysical Research*, *116*, A07227. <https://doi.org/10.1029/2010JA016355>
- Kletzing, C. A., Kurth, W. S., Acuna, M., MacDowall, R. J., Torbert, R. B., Averkamp, T., et al. (2013). The Electric and Magnetic Field Instrument Suite and Integrated Science (EMFISIS) on RBSP. *Space Science Reviews*, *179*(1), 127–181. <https://doi.org/10.1007/s11214-013-9993-6>
- Kozyra, J. U., Cravens, T. E., Nagy, A. F., Fontheim, E. G., & Ong, R. S. B. (1984). Effects of energetic heavy ions on electromagnetic ion cyclotron wave generation in the plasmopause region. *Journal of Geophysical Research*, *89*, 2217–2233. <https://doi.org/10.1029/JA089iA04p02217>
- Kuwashima, M., Toya, T., Kawamura, M., Hirasawa, T., Fukunishi, H., & Ayukawa, M. (1981). Comparative study of magnetic Pc1 pulsations between low latitudes and high latitudes: Statistical study. *National Institute Polar Research Memoirs*, *18*, 101.
- Lee, D.-Y., Shin, D.-K., & Choi, C.-R. (2018). Effects of oblique wave normal angle and noncircular polarization of electromagnetic ion cyclotron waves on the pitch angle scattering of relativistic electrons. *Journal of Geophysical Research: Space Physics*, *123*, 4556–4573. <https://doi.org/10.1029/2018JA025342>
- Lessard, M. R., Lindgren, E. A., Engebretson, M. J., & Weaver, C. (2015). Solar cycle dependence of ion cyclotron wave frequencies. *Journal of Geophysical Research: Space Physics*, *120*, 4711–4718. <https://doi.org/10.1002/2014JA020791>
- Lessard, M. R., Weatherwax, A. T., Spasojevic, M., Inan, U. S., Gerrard, A., Lanzerotti, L., et al. (2009). PENGUIn multi-instrument observations of dayside high-latitude injections during the 23 March 2007 substorm. *Journal of Geophysical Research*, *114*, A00C11. <https://doi.org/10.1029/2008JA013507>
- Li, Z., Millan, R. M., Hudson, M. K., Woodger, L. A., Smith, D. M., Chen, Y., et al. (2014). Investigation of EMIC wave scattering as the cause for the BARREL 17 January 2013 relativistic electron precipitation event: A quantitative comparison of simulation with observations. *Geophysical Research Letters*, *41*, 8722–8729. <https://doi.org/10.1002/2014GL062273>
- Li, J., Ni, B., Ma, Q., Xie, L., Pu, Z., Fu, S., et al. (2016). Formation of energetic electron butterfly distributions by magnetosonic waves via Landau resonance. *Geophysical Research Letters*, *43*, 3009–3016. <https://doi.org/10.1002/2016GL067853>
- Lundblad, J. A., & Soraas, F. (1978). Proton observations supporting the ion cyclotron wave heating theory of SAR arc formation. *Planetary and Space Science*, *26*, 245–254. [https://doi.org/10.1016/0032-0633\(78\)90090-9](https://doi.org/10.1016/0032-0633(78)90090-9)
- Lyons, L. R., & Thorne, R. M. (1972). Parasitic pitch angle diffusion of radiation belt particles by ion cyclotron waves. *Journal of Geophysical Research*, *77*, 5608–5616.
- McCollough, J. P., Elkington, S. R., & Baker, D. N. (2009). Modeling EMIC wave growth during the compression event of 29 June 2007. *Geophysical Research Letters*, *36*, L18108. <https://doi.org/10.1029/2009GL039985>
- McCollough, J. P., Elkington, S. R., & Baker, D. N. (2012). The role of Shabansky orbits in compression-related electromagnetic ion cyclotron wave growth. *Journal of Geophysical Research*, *117*, A01208. <https://doi.org/10.1029/2011JA016948>
- Meredith, N. P., Thorne, R. M., Horne, R. B., Summers, D., Fraser, B. J., & Anderson, R. R. (2003). Statistical analysis of relativistic electron energies for cyclotron resonance with EMIC waves observed on CRRES. *Journal of Geophysical Research*, *108*(A6), 1250. <https://doi.org/10.1029/2002JA009700>
- Min, K., Lee, J., & Keika, K. (2010). Chorus wave generation near the dawnside magnetopause due to drift shell splitting of substorm-injected electrons. *Journal of Geophysical Research*, *115*, A00102. <https://doi.org/10.1029/2010JA015474>
- Miyoshi, Y., Sakaguchi, K., Shiokawa, K., Evans, D., Albert, J., Connors, M., & Jordanova, V. (2008). Precipitation of radiation belt electrons by EMIC waves, observed from ground and space. *Geophysical Research Letters*, *35*, L23101. <https://doi.org/10.1029/2008GL035727>
- Morley, S. K., Friedel, R. H. W., Cayton, T. E., & Noveroske, E. (2010). A rapid, global and prolonged electron radiation belt dropout observed with the Global Positioning System constellation. *Geophysical Research Letters*, *37*, L06102. <https://doi.org/10.1029/2010GL042772>
- Popova, T. A., Yahnin, A. G., Yahnina, T. A., & Frey, H. (2010). Relation between sudden increases in the solar wind dynamic pressure, auroral proton flashes, and geomagnetic pulsations in the Pc1 range. *Geomagnetism and Aeronomy*, *50*, 568–575. <https://doi.org/10.1134/S0016793210050038>
- Remya, B., Sibeck, D. G., Halford, A. J., Murphy, K. R., Reeves, G. D., Singer, H. J., et al. (2018). Ion injection triggered EMIC waves in the Earth's magnetosphere. *Journal of Geophysical Research: Space Physics*, *123*, 4921–4938. <https://doi.org/10.1029/2018JA025354>
- Rodger, C. J., Hendry, A. T., Clilverd, M. A., Kletzing, C. A., Brundell, J. B., & Reeves, G. D. (2015). High-resolution in situ observations of electron precipitation-causing EMIC waves. *Geophysical Research Letters*, *42*, 9633–9641. <https://doi.org/10.1002/2015GL066581>

- Rodger, C. J., Raita, T., Clilverd, M. A., Seppälä, A., Dietrich, S., Thomson, N. R., & Ulich, T. (2008). Observations of relativistic electron precipitation from the radiation belts driven by EMIC waves. *Geophysical Research Letters*, *35*, L16106. <https://doi.org/10.1029/2008GL034804>
- Saikin, A. A., Zhang, J.-C., Smith, C. W., Spence, H. E., Torbert, R. B., & Kletzing, C. A. (2015). The dependence on geomagnetic conditions and solar wind dynamic pressure of the spatial distributions of EMIC waves observed by the Van Allen Probes. *Journal of Geophysical Research: Space Physics*, *121*, 4362–4377. <https://doi.org/10.1002/2016JA022523>
- Sakaguchi, K., Miyoshi, Y., Spanswick, E., Donovan, E., Mann, I. R., Jordanova, V., et al. (2012). Visualization of ion cyclotron wave and particle interactions in the inner magnetosphere via THEMIS-ASI observations. *Journal of Geophysical Research*, *117*, A10204. <https://doi.org/10.1029/2012JA018180>
- Sandanger, M., Søråas, F., Aarsnes, K., Oksavik, K., & Evans, D. S. (2007). Loss of relativistic electrons: Evidence for pitch angle scattering by electromagnetic ion cyclotron waves excited by unstable ring current protons. *Journal of Geophysical Research*, *112*, A12213. <https://doi.org/10.1029/2006JA012138>
- Shprits, Y. Y., Drozdov, A. Y., Spasojevic, M., Kellerman, A. C., Usanova, M. E., Engebretson, M. J., et al. (2016). Wave-induced loss of ultra-relativistic electrons in the Van Allen radiation belts. *Nature Communications*, *7*, 12883. <https://doi.org/10.1038/ncomms12883>
- Sibeck, D. G., McEntire, R. W., Lui, A. T. Y., Lopez, R. E., & Krimigis, S. M. (1987). Magnetic field drift shell splitting—Cause of unusual dayside particle pitch angle distributions during storms and substorms. *Journal of Geophysical Research*, *92*, 13,485–13,497.
- Spasojevic, M., & Fuselier, S. A. (2009). Temporal evolution of proton precipitation associated with the plasmaspheric plume. *Journal of Geophysical Research*, *114*, A12201. <https://doi.org/10.1029/2009JA014530>
- Spence, H. E., Reeves, G. D., Baker, D. N., Blake, J. B., Bolton, M., Bourdarie, S., et al. (2013). Science goals and overview of the Radiation Belt Storm Probes (RBSP) Energetic Particle, Composition, and Thermal Plasma (ECT) suite on NASA's Van Allen Probes Mission. *Space Science Reviews*, *179*(1), 311–336. <https://doi.org/10.1007/s11214-013-0007-5>
- Summers, D., & Thorne, R. M. (2003). Relativistic electron pitch-angle scattering by electromagnetic ion cyclotron waves during geomagnetic storms. *Journal of Geophysical Research*, *108*(A4), 1143. <https://doi.org/10.1029/2002JA009489>
- Summers, D., Thorne, R. M., & Xiao, F. (1998). Relativistic theory of wave-particle resonant diffusion with application to electron acceleration in the magnetosphere. *Journal of Geophysical Research*, *103*, 20,487–20,500. <https://doi.org/10.1029/98JA01740>
- Tetrick, S., Engebretson, M. J., Posch, J. L., Olson, C. N., Smith, C. W., Denton, R. E., et al. (2017). Location of intense electromagnetic ion cyclotron (EMIC) wave events relative to the plasmopause: Van Allen Probes observations. *Journal of Geophysical Research: Space Physics*, *122*, 4064–4088. <https://doi.org/10.1002/2016JA023392>
- Usanova, M. E., Drozdov, A., Orlova, K., Mann, I. R., Shprits, Y., Robertson, M. T., et al. (2014). Effect of EMIC waves on relativistic and ultrarelativistic electron populations: Ground-based and Van Allen Probes observations. *Geophysical Research Letters*, *41*, 1375–1381. <https://doi.org/10.1002/2013GL059024>
- Usanova, M. E., Mann, I. R., Bortnik, J., Shao, L., & Angelopoulos, V. (2012). THEMIS observations of electromagnetic ion cyclotron wave occurrence: Dependence on AE, SYMH, and solar wind dynamic pressure. *Journal of Geophysical Research*, *117*, A10218. <https://doi.org/10.1029/2012JA018049>
- Usanova, M. E., Mann, I. R., Kale, Z. C., Rae, I. J., Sydora, R. D., Sandanger, M., et al. (2010). Conjugate ground and multisatellite observations of compression-related EMIC Pc1 waves and associated proton precipitation. *Journal of Geophysical Research*, *115*, A07208. <https://doi.org/10.1029/2009JA014935>
- Usanova, M. E., Mann, I. R., Rae, I. J., Kale, Z. C., Angelopoulos, V., Bonnell, J. W., et al. (2008). Multipoint observations of magnetospheric compression-related EMIC Pc1 waves by THEMIS and CARISMA. *Geophysical Research Letters*, *35*, L17S25. <https://doi.org/10.1029/2008GL034458>
- Viall, N. M., Kepko, L., & Spence, H. E. (2009). Relative occurrence rates and connection of discrete frequency oscillations in the solar wind density and dayside magnetosphere. *Journal of Geophysical Research*, *114*, A01201. <https://doi.org/10.1029/2008JA013334>
- Wang, D., Yuan, Z., Deng, X., Zhou, M., Huang, S., Li, M., et al. (2014). Compression-related EMIC waves drive relativistic electron precipitation. *Science China Technological Sciences*, *57*, 2418–2425. <https://doi.org/10.1007/s11431-014-5701-3>
- Wang, D., Yuan, Z., Yu, X., Huang, S., Deng, X., Zhou, M., & Li, H. (2016). Geomagnetic storms and EMIC waves: Van Allen Probe observations. *Journal of Geophysical Research: Space Physics*, *121*, 6444–6457. <https://doi.org/10.1002/2015JA022318>
- Wilken, B., Baker, D. N., Higbie, P. R., Fritz, T. A., Olson, W. P., & Pfizter, K. A. (1986). Magnetospheric configuration and energetic particle effects associated with a SSC: A case study of the CDAW 6 Event on March 22, 1979. *Journal of Geophysical Research*, *91*(A2), 1459–1473. <https://doi.org/10.1029/JA091iA02p01459>
- Woodger, L. A., Halford, A. J., Millan, R. M., McCarthy, M. P., Smith, D. M., Bowers, G. S., et al. (2015). A summary of the BARREL campaigns: Technique for studying electron precipitation. *Journal of Geophysical Research: Space Physics*, *120*, 4922–4935. <https://doi.org/10.1002/2014JA020874>
- Woodger, L. A., Millan, R. M., Li, Z., & Sample, J. G. (2018). Impact of background magnetic field for EMIC wave-driven electron precipitation. *Journal of Geophysical Research: Space Physics*, *123*, 8518–8532. <https://doi.org/10.1029/2018JA025315>
- Xiao, F., Chen, L., He, Y., Su, Z., & Zheng, H. (2011). Modeling for precipitation loss of ring current protons by electromagnetic ion cyclotron waves. *Journal of Atmospheric and Solar-Terrestrial Physics*, *73*, 106–111. <https://doi.org/10.1016/j.jastp.2010.01.007>
- Xiao, F., Yang, C., Su, Z., Zhou, Q., He, Z., He, Y., et al. (2015). Wave-driven butterfly distribution of Van Allen belt relativistic electrons. *Nature Communications*, *6*, 8590. <https://doi.org/10.1038/ncomms9590>
- Yahnin, A. G., Yahnina, T. A., Frey, H. U., Börsinger, T., & Manninen, J. (2009). Proton aurora related to intervals of pulsations of diminishing periods. *Journal of Geophysical Research*, *114*, A12215. <https://doi.org/10.1029/2009JA014670>
- Yahnina, T. A., Yahnin, A. G., Kangas, J., & Manninen, J. (2000). Proton precipitation related to Pcl pulsations. *Geophysical Research Letters*, *27*, 3575–3578. <https://doi.org/10.1029/2000GL003763>
- Yuan, Z., Deng, X., Lin, X., Pang, Y., Zhou, M., Décréau, P. M. E., et al. (2010). Link between EMIC waves in a plasmaspheric plume and a detached sub-auroral proton arc with observations of Cluster and IMAGE satellites. *Geophysical Research Letters*, *37*, L07108. <https://doi.org/10.1029/2010GL042711>
- Yuan, Z., Liu, K., Yu, X., Yao, F., Huang, S., Wang, D., & Ouyang, Z. (2018). Precipitation of radiation belt electrons by EMIC waves with conjugated observations of NOAA and Van Allen Satellites. *Geophysical Research Letters*, *45*, 12,694–12,702. <https://doi.org/10.1029/2018GL080481>